The Astrophysical Journal, 955:26 (14pp), 2023 September 20 https://doi.org/10.3847/1538-4357/ace773

Constraining Cosmological Parameters Using the Cluster Mass–Richness Relation

Mohamed H. Abdullah[1,2], Gillian Wilson[3,4], Anatoly Klypin[5,6], and Tomoaki Ishiyama[1]
[1] Digital Transformation Enhancement Council, Chiba University, 1-33, Yayoi-cho, Inage-ku, Chiba, 263-8522, Japan; melha004@ucr.edu
[2] Department of Astronomy, National Research Institute of Astronomy and Geophysics, Cairo, 11421, Egypt
[3] Department of Physics and Astronomy, University of California Riverside, 900 University Avenue, Riverside, CA 92521, USA
[4] Department of Physics, University of California Merced, 5200 Lake Road, Merced, CA 95343, USA
[5] Astronomy Department, New Mexico State University, Las Cruces, NM 88001, USA
[6] Department of Astronomy, University of Virginia, Charlottesville, VA 22904, USA
Received 2022 October 16; revised 2023 July 12; accepted 2023 July 12; published 2023 September 13

Abstract

The cluster mass–richness relation (MRR) is an observationally efficient and potentially powerful cosmological tool for constraining the matter density Ω_m and the amplitude of fluctuations σ_8 using the cluster abundance technique. We derive the MRR relation using `GalWCat19`, a publicly available galaxy cluster catalog we created from the Sloan Digital Sky Survey-DR13 spectroscopic data set. In the MRR, cluster mass scales with richness as $\log M_{200} = \alpha + \beta \log N_{200}$. We find that the MRR we derive is consistent with both the IllustrisTNG and mini-Uchuu cosmological numerical simulations, with a slope of $\beta \approx 1$. We use the MRR we derived to estimate cluster masses from the `GalWCat19` catalog, which we then use to set constraints on Ω_m and σ_8. Utilizing the all-member MRR, we obtain constraints of $\Omega_m = 0.31^{+0.04}_{-0.03}$ and $\sigma_8 = 0.82^{+0.05}_{-0.04}$, and utilizing the red member MRR only, we obtain $\Omega_m = 0.31^{+0.04}_{-0.03}$ and $\sigma_8 = 0.81^{+0.05}_{-0.04}$. Our constraints on Ω_m and σ_8 are consistent and very competitive with the Planck 2018 results.

Unified Astronomy Thesaurus concepts: Galaxy clusters (584); Cosmological parameters (339); Galaxy cluster counts (583)

1. Introduction

In the current paradigm of structure formation, galaxy clusters arise from rare high peaks of the initial density fluctuation field. These peaks grow in a hierarchical fashion through the dissipationless mechanism of gravitational instability with more massive haloes growing via continued accretion and merging of low-mass haloes (White & Frenk 1991; Kauffmann et al. 1999, 2003). Galaxy clusters are the most massive virialized systems in the universe and are uniquely powerful cosmological probes. The cluster mass function (CMF[7]), or the abundance of galaxy clusters, is particularly sensitive to the matter density of the universe (Ω_m) and the rms mass fluctuation on the scale of 8 h^{-1} Mpc (σ_8) (e.g., Wang & Steinhardt 1998; Battye & Weller 2003; Dahle 2006; Wen et al. 2010).

The main challenge in utilizing cluster abundances to constrain Ω_m and σ_8 lies in accurately estimating the mass of each cluster. Cluster mass is not a directly observable quantity but, fortunately, can be inferred indirectly from other observables, the so-called mass proxies, which do scale tightly with cluster mass. Among these mass proxies are X-ray luminosity, X-ray temperature, the product of X-ray temperature and gas mass (e.g., Pratt et al. 2009; Vikhlinin et al. 2009; Mantz et al. 2016), optical luminosity (e.g., Yee & Ellingson 2003), and the velocity dispersion of cluster members (e.g., Biviano et al. 2006; Bocquet et al. 2015). Of particular note is cluster richness (the total number of members with a luminosity greater than some given luminosity threshold). This mass proxy has been extensively used in the literature (e.g., Abbott et al. 2020; Pereira et al. 2018), and is commonly referred to as the mass–richness relation (hereafter MRR).

Another challenge to accurately determining the values of Ω_m and σ_8 is the well-known degeneracy between those two parameters. Figure 1 illustrates this degeneracy, showing the effect on the cluster abundance and mass if either the value of Ω_m or σ_8 is held fixed while the other is varied. We use the functional form of the halo mass function from Tinker et al. (2008) to calculate the halo mass function (HMF; see Table 1 for a list of abbreviations used in this paper) and then plot the expected number of clusters and their masses within a fixed volume. As shown in Figure 1, increasing Ω_m while holding σ_8 fixed i.e., moving from left to right across the top row, results in an increasing number of clusters of all masses. Increasing σ_8 while holding Ω_m fixed, i.e., moving from left to right across the bottom row, also results in an increasing number of clusters of all masses. Interestingly, however, as shown in the lower right panel, increasing σ_8 while holding Ω_m fixed increases the number of high-mass clusters more dramatically than the number of low-mass clusters. In other words, the high-mass end of the HMF is very sensitive to σ_8.

Large wide and deep-field imaging and spectroscopic galaxy surveys, such as DES (Abbott et al. 2018), DESI (Levi et al. 2019), Euclid (Adam et al. 2019), eROSITA (Merloni et al. 2012), the LSST that will be carried out on the Vera C. Rubin Observatory (Abell et al. 2009), the High Latitude Wide Area Survey that will be carried out on the Nancy Grace Roman Telescope (Akeson et al. 2019), SPHEREX (Doré et al. 2014), and the Subaru Prime Focus Spectrograph (PFS; Takada et al. 2014) will collectively and simultaneously increase the

[7] Throughout the paper we use CMF for the mass function derived from observations and HMF (see Table 1) for the mass function computed by analytic models.

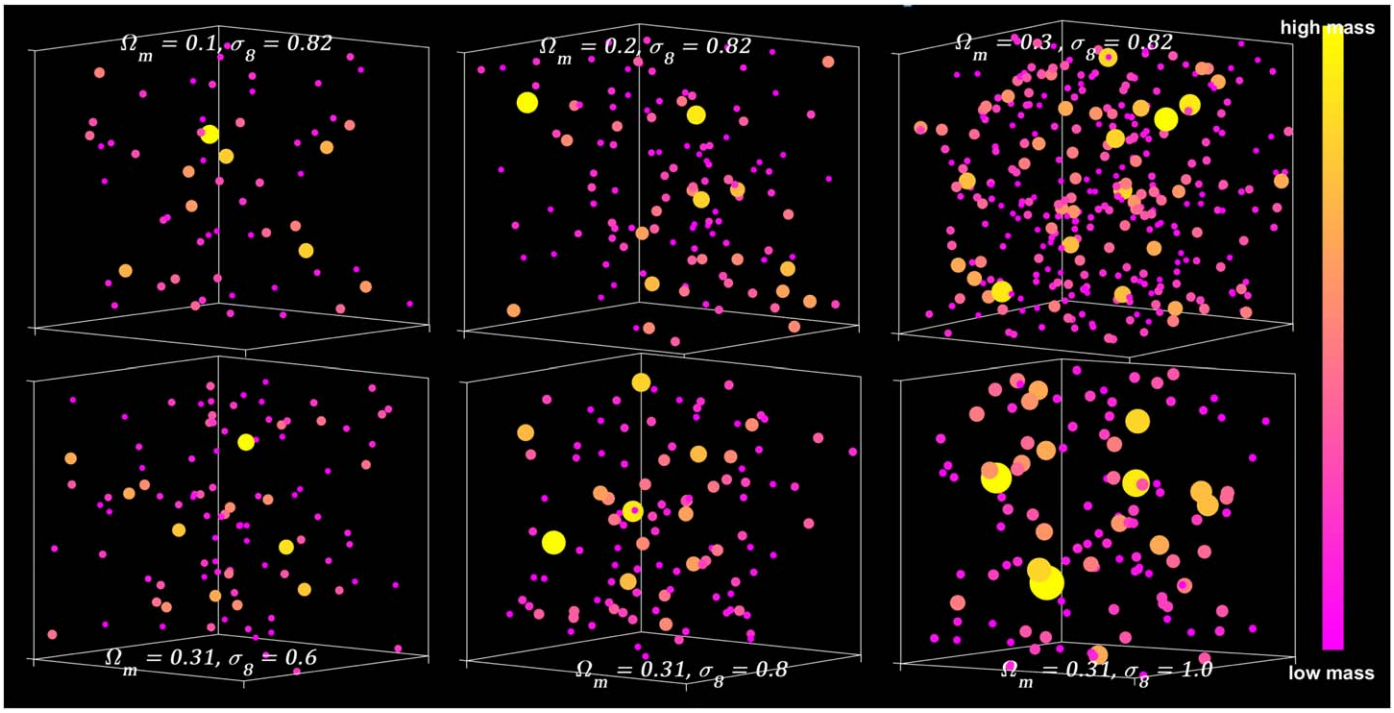

Figure 1. Schematic diagram showing the effect on the cluster abundance by varying either Ω_m (upper) or σ_8 (lower) while holding the other parameter fixed. Each circle represents a cluster with its size (large to small) and color (yellow to magenta) indicating high to low mass. Increasing Ω_m results in an approximately proportionally higher number of clusters of every mass. Increasing σ_8 also results in a higher number of clusters of every mass but also changes the ratio of high-to-low-mass clusters, so results in a larger number of high-mass clusters relative to low-mass clusters. Note that the clusters are distributed randomly in each box.

Table 1
List of Abbreviations Used in This Paper

Abbreviation	Definition
MRR	Mass–richness relation
$\mathrm{MRR_{all}}$	Mass–richness relation derived for all member galaxies within R_{200}
$\mathrm{MRR_{red}}$	Mass–richness relation derived for red member galaxies within R_{200}
α	Normalization of the mass–richness relation
β	Slope of the mass–richness relation
$\sigma_{\rm int}$	Intrinsic scatter in the mass–richness relation
$N_{\rm th}$	Richness threshold
$\mathcal{S}_{\rm fid}$	A fiducial subsample of 756 clusters with $\log M_{200} \geqslant 13.9$ $[h^{-1}\,M_\odot]$ and $0.045 \leqslant z \leqslant 0.125$
$\mathcal{S}\mathrm{all}_{17}$	A fiducial subsample of clusters with $\log M_{200} \geqslant 13.9$ $[h^{-1}\,M_\odot]$, $0.045 \leqslant z \leqslant 0.125$, and $N_{\rm th} = 17$ for all members within R_{200}
$\mathcal{S}\mathrm{red}_{13}$	A fiducial subsample of clusters with $\log M_{200} \geqslant 13.9$ $[h^{-1}\,M_\odot]$, $0.045 \leqslant z \leqslant 0.125$, and $N_{\rm th} = 13$ for red members within R_{200}
$f_{\rm x}$	Fractional scatter defined as $f_x = (x - x_{\rm fid})/x_{\rm fid}$, and x, and $x_{\rm fiid}$ are the estimated and fiducial parameters
MCMC	Markov chain Monte Carlo
CMF	Cluster mass function
HMF	Halo mass function
$\mathrm{CMF_{MRR}}$	Deriving constraints on $\Omega_{\rm m}$ and σ_8 using the cluster abundance technique and cluster mass estimates from the mass–richness relation
$\mathrm{CMF_{dyn}}$	Deriving constraints on $\Omega_{\rm m}$ and σ_8 using the cluster abundance technique and cluster mass estimates from the dynamics of member galaxies
CMB	Deriving constraints on $\Omega_{\rm m}$ and σ_8 using the cosmic microwave background radiation (CMB) technique

precision of the constraints on $\Omega_{\rm m}$ and σ_8, break the degeneracy between them, and also constrain additional cosmological parameters such as dark energy Ω_Λ, and the equation of state ω (e.g., Rozo et al. 2010; Weinberg et al. 2013; Aghanim et al. 2020).

The MRR is an observationally cheap but potentially powerful cosmological tool. For any galaxy cluster catalog that contains photometry but lacks an estimate of cluster masses, the mass of each cluster can be estimated using the MRR relation. These cluster mass estimates can then be used to derive the CMF and hence to constrain the values of $\Omega_{\rm m}$ and σ_8. Hereafter in this paper, we refer to the application of this technique as $\mathrm{CMF_{MRR}}$.

The $\mathrm{CMF_{MRR}}$ technique has previously been applied to a number of photometric galaxy cluster catalogs (e.g., Rozo et al. 2010; Costanzi et al. 2019; Kirby et al. 2019; Lesci et al. 2022). However, the constraints on $\Omega_{\rm m}$ and σ_8 derived from these previous works using the $\mathrm{CMF_{MRR}}$ technique have been shown to be in tension with each other (see Abdullah et al. 2020a). This is likely because large systematics tend to be introduced when cluster catalogs are constructed from imaging observations. The reasons for this are multiple. First, distances inferred

from photometric redshift estimates are less accurate than those inferred from spectroscopic redshifts. This increases the incidence of line-of-sight galaxies in close projection that are falsely assigned to be cluster members. Second, cluster catalogs constructed from photometric surveys do not return an estimate of the mass of each cluster. For such photometric samples, the cluster mass must be inferred indirectly from the optical richness. To estimate the mass of each cluster in a photometric catalog, a subset of clusters is commonly followed up in more detail and their masses are calculated individually using a technique such as weak lensing or X-ray observations. Cluster mass can also be estimated collectively by stacking clusters in a series of richness bins and estimating the mean mass for each bin from the stacked weak lensing mass profile (e.g., Simet et al. 2017). The MRR can, therefore, be determined from the subsample and then applied to the full catalog. As a result, as we discuss in more detail below and illustrate in Figure 3, the MRRs and cosmological parameters derived from these previous analyses (e.g., Johnston et al. 2007; Wiesner et al. 2015; Melchior et al. 2017) are in tension with each other, even in the case of analyses that use the same cluster sample. We believe these to be the reasons for the discrepancies among the cosmological parameters derived (see Figure 7 in Abdullah et al. 2020a and Figure 4 in this paper).

In this paper, we wish to demonstrate the feasibility of recovering accurate cosmological constraints given a reliable MRR. To do this we obtain the MRR by utilizing the spectroscopic GalWCat19 cluster catalog for which photometry also exists. We only use the spectroscopically derived cluster dynamical mass estimates to obtain the MRR. We do not subsequently utilize the dynamical masses but rather only the MRR to (re-)estimate the mass of each cluster, determine the CMF and constrain cosmological parameters. This approach enables us to demonstrate that a well-determined MRR is the key to attaining robust and competitive constraints on $\Omega_{\rm m}$ and σ_8. It also allows us to quantify both the scatter in the MRR and any potential systematic effects.

In the first part of the paper, we derive the MRR, the relationship between dynamical mass and optical richness. The MRR is derived for two cases: first, by considering all members within R_{200}[8] (hereafter $\rm MRR_{all}$) and second by considering only the red galaxy members within R_{200} (hereafter $\rm MRR_{red}$). Red galaxy members are identified using the red-sequence region in the color–magnitude diagram (CMD; e.g., Hao et al. 2009, see Appendix A). In the second part of the paper, we utilize each MRR independently to estimate cluster mass based on optical richness. We then construct the cluster mass function and employ the cluster abundance technique to obtain constraints on $\Omega_{\rm m}$ and σ_8. We utilize each of the two MRRs independently and compare the resulting cosmological constraints to each other as well as to constraints from the literature.

This paper is organized as follows. In Section 2, we briefly describe the GalWCat19 cluster catalog, which we use in deriving the MRR. We discuss how we determine the completeness of the catalog as a function of mass and redshift, and how we determine the richness of each cluster. In Section 3, we describe the basic ingredients and methodology of the MRR analysis and present our estimates of the MRR parameters. In Section 4, we present our constraints on $\Omega_{\rm m}$ and σ_8 and compare our results with those from previous works. We summarize our conclusions and future work in Section 5. Throughout the paper, we adopt a Lambda cold dark matter (ΛCDM) cosmology with $\Omega_{\rm m} = 1 - \Omega_\Lambda$, and $H_0 = 100\,h$ km s^{-1} Mpc^{-1}. Note that throughout the paper we write log as shorthand for $\log_{10}$.

2. Data

2.1. The GalWCat19 Cluster Catalog

In this section, we summarize how we created the GalWCat19 cluster catalog. Full details can be found in Abdullah et al. (2020b). Using both the photometric and spectroscopic data sets from the Sloan Digital Sky Survey (SDSS) DR13, we extracted data for all galaxies that satisfied the following set of criteria: spectroscopic detection, photometric, and spectroscopic classification as a galaxy (by the automatic pipeline), spectroscopic redshift between 0.001 and 0.2 (with a redshift completeness >0.7, Yang et al. 2007, Tempel et al. 2014), and r-band magnitude (reddening-corrected) <18, flag SpecObj.zWarning = zero (indicating a well-measured redshift). This resulted in a catalog containing 704,200 galaxies that satisfied all of the criteria.

Galaxy clusters were identified by the well-known Fingers-of-God effect (Jackson 1972; Kaiser 1987; Abdullah et al. 2013). We applied the binary tree algorithm (e.g., Serra et al. 2011) to accurately determine the cluster center and a phase-space diagram. Galaxy membership for each cluster was assigned by applying the GalWeight technique (developed by our group and presented in Abdullah et al. 2018) to galaxies in the phase-space diagram out to a maximum projected radius of $10\,h^{-1}$ Mpc and within a maximum line-of-sight velocity range of ± 3000 km s^{-1}. In Abdullah et al. (2018), using the Bolshoi simulation (Klypin et al. 2016), we showed that GalWeight was ∼98% accurate in assigning cluster membership for clusters with mass $M_{200} > 2 \times 10^{14}\,h^{-1} M_\odot$ and ∼85% for clusters with mass $M_{200} > 0.4 \times 10^{14}\,h^{-1} M_\odot$.

After applying GalWeight to determine cluster membership, the virial mass of each cluster was estimated. This was done by applying the virial theorem under the assumption that the mass distribution follows the galaxy distribution (e.g., Giuricin et al. 1982; Merritt 1988). The estimated mass was then corrected for the surface pressure term which, otherwise, would overestimate the true cluster mass (e.g., The & White 1986; Binney & Tremaine 1987). The cluster virial mass was calculated at the viral radius within which the cluster is in hydrostatic equilibrium. The virial radius is approximately equal to the radius within which the density $\rho = \Delta_{200}\rho_c$, where ρ_c is the critical density of the universe and $\Delta_{200} = 200$ (e.g., Carlberg et al. 1997; Klypin et al. 2016). Abdullah et al. (2020b) showed that the cluster mass estimates returned by the virial theorem compared very favorably to other commonly utilized mass estimation techniques, which were described and compared in Old et al. (2015).

The GalWCat19 catalog is publicly available.[9] As described in Abdullah et al. (2020b), it consists of two tables, one characterizing the clusters and another characterizing the member galaxies. In creating the GalWCat19 catalog, a ΛCDM cosmology with $\Omega_{\rm m} = 1 - \Omega_\Lambda$ and $H_0 = 100\,h$ km s^{-1} Mpc^{-1} was assumed. The cluster table has 1800 clusters with

[8] Throughout the paper we assume R_{200} is the virial radius of the cluster and M_{200} is the virial mass enclosed within R_{200}. In practice, the virial radius at which the cluster is in hydrostatic equilibrium cannot be determined. We follow convention and assume that the virial radius R_{200} is the radius within which the average density $\langle \rho(r < R_{200}) \rangle = 200\rho_c$, where ρ_c is the critical density of the universe.

[9] http://cdsarc.u-strasbg.fr/viz-bin/cat/J/ApJS/246/2

redshifts in the range of $0.01 < z < 0.2$ and total masses in the range of (0.4–14) $\times$ 10^{14} h^{-1} $M_{\odot}$. The cluster table also contains the coordinates of each cluster on the sky (R.A., decl.), redshift, number of members, velocity dispersion, and dynamical mass within four overdensities ($\Delta = 500$, 200, 100, 5.5). Note that merging clusters have been removed. The GalWCat19 galaxy member table contains 34,471 members that were identified to lie within each cluster's virial radius at which the density is 200 times the critical density of the universe. The galaxy member table contains the coordinates of each cluster member and the ID of the host cluster.

In the remainder of this paper, we will primarily focus on analyzing the GalWCat19 cluster table and will utilize the GalWCat19 galaxy member table only to calculate the richness of each cluster (see Section 3). For brevity, therefore, hereafter when we refer to the GalWCat19 catalog, we are referring to the GalWCat19 cluster table.

2.2. Completeness Corrections

Abdullah et al. (2020a) showed that GalWCat19 is incomplete in redshift at $z > 0.085$ but that it was possible to correct for this incompleteness in redshift if each cluster at $z > 0.085$ was weighted by a selection function given by

$$\mathcal{S}_z(D) = 1.07 \exp\left[-\left(\frac{D}{293.4}\right)^{2.97}\right], \quad (1)$$

where D is the comoving distance to the cluster, and with the condition that $\mathcal{S}_z \leqslant 1$. Thus, the weight that is applied to any given cluster at redshift z is $\mathcal{W}_z = 1/\mathcal{S}_z(D)$. Caution is advised in using $\mathcal{S}_z$ to weight those clusters which are at higher redshift in the GalWCat19 catalog. This is because above a redshift threshold, the weight becomes disproportionately large and introduces a high scatter and bias in the CMF toward the highest redshift clusters in the catalog. Thus, in order to avoid these effects we restrict our sample to a maximum redshift of $z = 0.125$.

Abdullah et al. (2020a) also showed that the value of mass at which the catalog is complete depends slightly on the cosmology, but that GalWCat19 is approximately complete for clusters with masses of $\log(M) \geqslant 13.9\ h^{-1}\,M_{\odot}$. If we apply the above redshift incompleteness correction and restrict our sample to clusters with redshifts of $0.045 \leqslant z \leqslant 0.125$ and masses of $\log(M) \geqslant 13.9\ h^{-1}\,M_{\odot}$, a total of 756 clusters remain (≈42% of the GalWCat19 sample). We call this fiducial subsample of clusters, $\mathcal{S}_{\rm fid}$. Thus, the fiducial subsample comprises clusters with more reliable mass and redshift estimates, which we will utilize to effectively constrain cosmological parameters. In Section 4.3, we discuss the systematics introduced by adopting these redshift and mass thresholds on our best-fit estimates of $\Omega_{\rm m}$ and σ_8.

2.3. Richness

In this section, we discuss how we calculate the richness of each cluster. For each cluster member, we calculate the absolute magnitude in the r band, $M_{\rm r}$, using

$$M_r - 5\log h = m_r - DM(z) - K(z) - E(z), \quad (2)$$

where $DM(z) = 5\log D_L - 5\log h - 25$ is the distance modulus calculated from the luminosity distance D_L, $M_{\rm r}$ is the AB apparent magnitude in the r-band calculated from the SDSS magnitude using $m_{AB} = m_{sdss} + 0.010$, $K(z)$ is the K-correction, calculated using the latest version of "Kcorrect" (v4), and $E = Q(z - 0.1)$, where $Q = -1.62$ is the evolutionary correction in the r band (see Blanton et al. 2003; Blanton & Roweis 2007 for details). Absolute magnitudes are $K(z)$ and $E(z)$ corrected to redshift $z = 0.1$, which is approximately equal to the mean redshift of the GalWCat19 catalog ($z = 0.089$).

We define the richness of each cluster, N_{200}, as the total number of members with luminosity $L \geqslant 0.4L^{*}$ within R_{200}. L^{*} is the redshift-dependent characteristic luminosity of a galaxy in the r band, which is defined as $L^{*}(z) = L^{*}(z = 0.1)10^{Q(z-0.1)}$. $L^{*}(z = 0.1)$ is equivalent to a characteristic absolute magnitude of $M_r^{*} = -20.44$ in the r band (Blanton et al. 2003) and a stellar mass of $\sim 5 \times 10^{9}\ h^{-1}\,M_{\odot}$ at $z = 0.1$ (Deason et al. 2019).

While the GalWeight technique has been shown to be effective at removing foreground/background galaxies (Abdullah et al. 2018), some interlopers that are embedded in the cluster field due to the triple-value problem (see Tonry & Davis 1981; Abdullah et al. 2020b) still remain in the GalWCat19 catalog and these need to be removed before the MRR can be constructed. As discussed in Abdullah et al. (2018), the percentage of these interlopers is about 11%. The total number of galaxies in the cluster, $N_{\rm tot}$, is equal to the number of members within R_{200}, N_{200}, plus the number of interlopers, $N_{\rm int}$. In order to remove contamination by these interlopers we calculated the surface density profile of each cluster from its center and fit it with the King equation, defined as

$$\Sigma_{\rm tot}(R) = \Sigma_c\left(1 + \frac{R^2}{r_c^2}\right)^{\nu} + \Sigma_{\rm int}, \quad (3)$$

where Σ_c and $\Sigma_{\rm int}$ are the central surface number density and interloper surface number density, respectively, and r_c is a core radius. We apply Equation (3) to all members assigned by the GalWeight technique within 6 h^{-1} Mpc of the cluster center. This is a sufficiently large radius to fit for the interloper surface number density $\Sigma_{\rm int}$ and estimate $N_{\rm int}$. We then subtract $N_{\rm int}$ from $N_{\rm tot}$ to get N_{200}.

The gray points in the left panel of Figure 2 show the distribution of all 1800 clusters in the GalWCat19 catalog in the mass–richness plane. Visual inspection shows that there is a large scatter in the relationship between mass and richness at the low-richness end. This is due to the large uncertainties introduced when calculating each cluster mass using a dynamical method in the case where only a handful of member galaxy redshifts are available. In contrast to the gray points, which show all clusters, the black points show the fiducial sample. The black points show the complete fiducial ($\mathcal{S}_{\rm fid}$) subsample of 756 clusters to which the redshift selection function has been applied ($\log M_{200} \geqslant 13.9\ h^{-1}\,M_{\odot}$ and $0.045 \leqslant z \leqslant 0.125$; see Section 2.2). The mean cluster mass as a function of richness in $\mathcal{S}_{\rm fid}$ is shown by the solid red circles. Visual inspection of the relationship between cluster mass and richness shown by the solid red circles in the left panel of Figure 2 reveals an intriguing relationship. At the high-richness end, the relationship is linear with a steep slope. However, as we move toward lower richness, a noticeable transition occurs, whereby the slope appears to become shallow i.e., exhibits a *tail*. There is a characteristic richness threshold below which

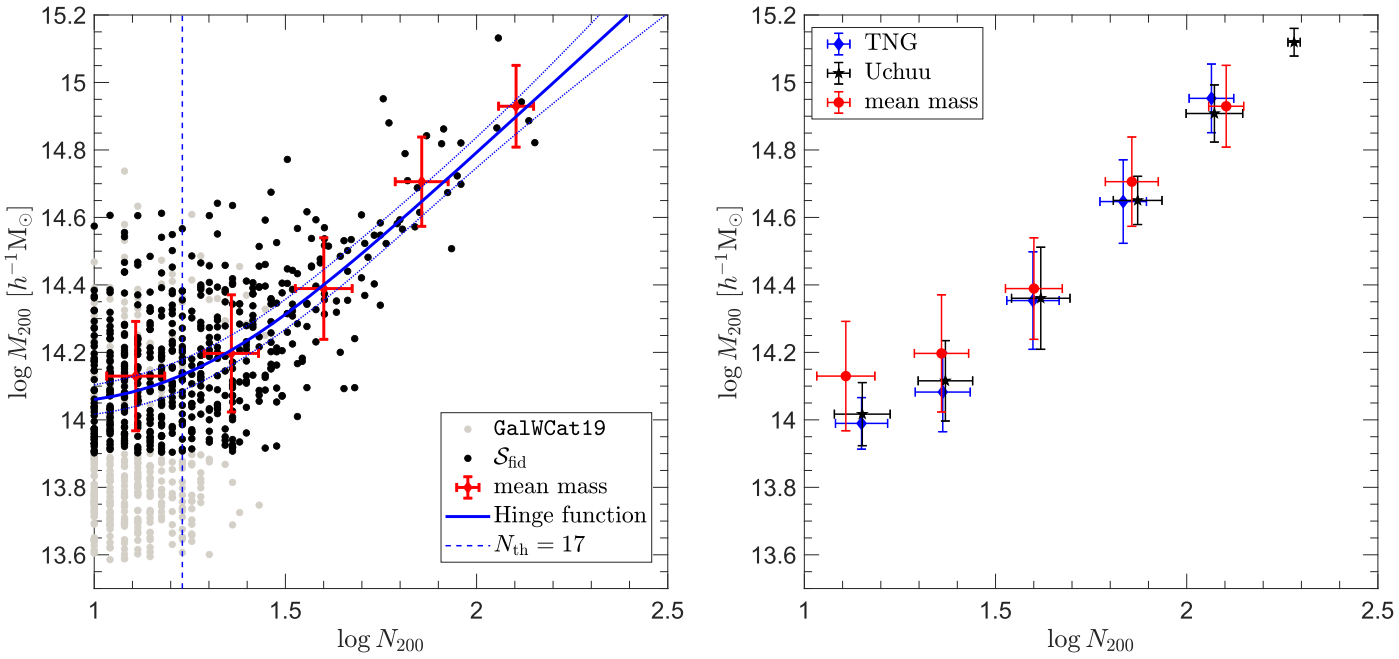

Figure 2. Left: distribution of clusters from the GalWCat19 catalog in the mass–richness plane. Gray points show all 1800 clusters (with a mass of $\log M_{200} \geqslant 13.5\ h^{-1}\,M_\odot$ and at a redshift $z \leqslant 0.2$ (see Section 2.3). Black points show the complete fiducial subsample ($\mathcal{S}_{\rm fid}$) of 756 clusters to which the redshift selection function has been applied ($\log M_{200} \geqslant 13.9\ h^{-1}\,M_\odot$ and $0.045 \leqslant z \leqslant 0.125$; see Section 2.2). The mean cluster mass as a function of richness in $\mathcal{S}_{\rm fid}$ is shown by the solid red circles, with the error bars indicating 1σ Poisson uncertainties. The blue solid line shows the Hinge function for $\mathcal{S}_{\rm fid}$ (see Section 2.5), with the dotted blue lines indicating 1σ uncertainties. The vertical blue dashed line shows the richness threshold at which the slope of the distribution changes (see Section 2.4 and Equation (4)). Right: red circles and uncertainties are as on the left. Also shown are the mean masses of clusters from two simulations (see 2.4). Black points show clusters from mini-Uchuu with a subhalo peak velocity threshold of $v_{\rm peak} = 130$ km s^{-1} and blue points show clusters from TNG with a galaxy stellar mass threshold of $M_s \geqslant 5 \times 10^9\ h^{-1}\,M_\odot$. As can be seen clearly from both panels, a flattening (tail) of the MRR occurs at low richness ($\log N \lesssim 1.23$). The short tail in the simulations is not intrinsic. It is partially due to the threshold of simulations as well as Poisson scattering (see Appendix B).

the slope of the relationship changes. Throughout the rest of this paper, we will refer to this characteristic threshold as $N_{\rm th}$.

In the following subsection, by analyzing two different state-of-the-art numerical simulations we demonstrate that this tail is not intrinsic. Furthermore, we present a technique to identify the optimal richness threshold, ($N_{\rm th}$), below which clusters should be discarded prior to deriving the MRR. This threshold is dependent on the cluster catalog being utilized, e.g., Baxter et al. (2016) and Murata et al. (2019) adopted $N_{\rm th} = 20$ for the redMaPPer cluster catalog (Rykoff et al. 2016) which utilizes red member galaxies, photometrically selected from the SDSS-DR8 catalog. In Section 2.5, we show how to apply a Hinge function to optimally determine $N_{\rm th}$ appropriate for any catalog. Using this method, we derive an optimal threshold of $N_{\rm th} = 17$ (13) for all (red) member galaxies in the GalWCat19 catalog.

2.4. Simulations

As discussed in Section 2.3, the MRR derived from the GalWCat19 cluster catalog reveals a tail at the low-richness end. In this section, we analyze two different simulations to demonstrate that this tail is not intrinsic. The first simulation is the TNG300-1 simulation from the IllustrisTNG300 suite (Pillepich et al. 2018; Nelson et al. 2019). The TNG300-1 simulation contains 2500^3 dark matter (DM) particles and the same number of baryonic resolution elements in a box of comoving length 205 h^{-1} Mpc. It evolves from redshift $z = 127$ down to $z = 0$ using the AREPO moving-mesh code (Springel 2010; Weinberger et al. 2020), which solves the coupled equations of ideal magnetohydrodynamics and self-gravity, taking magnetic fields into consideration. It assumes a standard ΛCDM cosmology, with $\Omega_\Lambda = 0.691$, $\Omega_{\rm m} = 0.309$, $\Omega_b = 0.0486$, $h = 0.6777$, $n_s = 0.9667$, and $\sigma_8 = 0.8159$ (Ade et al. 2016). The dark matter mass resolution is $4.0 \times 10^7\ h^{-1}\,M_\odot$ and the baryonic mass resolution is $0.75 \times 10^7\ h^{-1}\,M_\odot$. The gravitational softening lengths for dark matter and stars in TNG300-1 are $1.0\ h^{-1}$ kpc. In this study, we use snapshot #92 at redshift = 0.08, which most closely matches the mean redshift ($z = 0.089$) of clusters in the GalWCat19 catalog.

The second simulation is the mini-Uchuu simulation from the Uchuu suite of large, high-resolution N-body simulations (Ishiyama et al. 2021), which were done for the Planck2016 cosmology (Ade et al. 2016). Mini-Uchuu is a cosmological N-body simulation of 2560^3 particles in a box of comoving length 400 h^{-1} Mpc, mass resolution of $3.27 \times 10^8\ h^{-1}\,M_\odot$, and gravitational softening length of 4.27 h^{-1} kpc. Mini-Uchuu was created using the massively parallel N-body TreePM code, GREEM (Ishiyama et al. 2009, 2012). Haloes and subhaloes were identified with ROCKSTAR (Behroozi et al. 2013a) and merger trees constructed with CONSISTENT TREES (Behroozi et al. 2013b). Halo/subhalo catalogs and their merger trees are publicly available through the Skies & Universes site.[10] Full details of the Uchuu simulation suite may be found in Ishiyama et al. (2021). Here, we analyze a snapshot at redshift $z \sim 0.09$. Note that in order to be consistent with how the GalWCat19 cluster masses are calculated, in the case of both simulations we define the cluster mass M_{200} as the mass enclosed within an overdensity of $200\rho_c$, where ρ_c is the critical density of the universe.

[10] http://www.skiesanduniverses.org/Simulations/Uchuu/

The right panel of Figure 2 shows the MRR obtained from the IllustrisTNG (blue) and mini-Uchuu (black) simulations, as well as from the fiducial GalWCat19 cluster catalog, $\mathcal{S}_{\rm fid}$ (red). For the mini-Uchuu simulations, we count all subhaloes (galaxies) with a threshold of peak velocity $v_{\rm peak} = 130$ km s^{-1} (equivalent to the stellar mass of $\sim M_s = 5 \times 10^9\ h^{-1}\,M_\odot$ and luminosity $\sim 0.4 L_*$). For the IllustrisTNG haloes (clusters) we determine the number of galaxies with a threshold of stellar mass $M_s = 5 \times 10^9\ h^{-1}\,M_\odot$ within r_{200}. Note that for both simulations we select all clusters with mass $\log M_{200} \geqslant 13.9\ h^{-1}\,M_\odot$. As can be seen from the right panel, there is very good agreement between the GalWCat19 MRR and those derived from both Uchuu and TNG at high richness ($N \gtrsim 17$, or $\log N \geqslant 1.23$). However, as can also clearly be seen from the right panel, a flattening (tail) of the MRR occurs for both simulations at low richness ($\log N \leqslant 1.23$). In Appendix B, we show that the length of the tail for both simulations depends on the adopted $v_{\rm peak}$ or M_s thresholds. This indicates that the tail is an artifact introduced by the selection applied ($v_{\rm peak}$, or equivalently M_s), and is, therefore, not real. It is partially due to the threshold of simulations as well as Poisson scattering

Thus, the tail in the MRR obtained from GalWCat19 is not intrinsic and the effect at low richness is due to the Poisson scattering, the systematics of determining the member galaxies and richness, calculating cluster masses of a small members galaxies, and the projection effect. We note that there is a very good agreement with MRR obtained from GalWCat19 and both Uchuu and TNG at $N \gtrsim 17$. We conclude that it is necessary to apply a cut in richness. In Section 2.5, we describe a process for determining the optimal value of richness at which to make the cut.

2.5. Selecting the Richness Threshold

We wish to determine the optimal richness threshold to apply in order to remove the effect of the tail described in Section 2.4 and Figure 2. The MRR can then be derived for all clusters with richness larger than this threshold value. In order to find $N_{\rm th}$ below which the slope of MRR becomes artificially shallower we use the Hinge function (also known as a smoothed broken power law, e.g., Beuermann et al. 1999; Mowla et al. 2019; Baes & Camps 2021) defined as

$$Y = a + b_0(X - X_0) + (b - b_0)\,\delta \log\left(1 + \exp\frac{X - X_0}{\delta}\right), \quad (4)$$

where $Y = \log M_{200}$ and $X = \log N_{200}$. We use this function only to determine X_0, which in our case is the richness threshold $N_{\rm th}$.

Applying the Hinge function to the fiducial sample, $\mathcal{S}_{\rm fid}$ (Section 2.5), we find that the threshold at which the MRR changes its slope is $N_{\rm th} = 17$ for all members and $N_{\rm th} = 13$ for red members. In Appendix C, we discuss the effect on the MRR relation of varying the optimal richness threshold. The blue solid line in the left panel of Figure 2 shows the Hinge function calculated for $\mathcal{S}_{\rm fid}$ and using all cluster members, with the dotted blue lines indicating 1σ uncertainties. The vertical blue dashed line shows the optimal richness threshold of $N_{\rm th} = 17$, derived for all members. In summary, in order to derive MRR and cosmological constraints on $\Omega_{\rm m}$ and σ_8, we select all clusters with $\log M_{200} \geqslant 13.9$ $[h^{-1}\,M_\odot]$, $0.045 \leqslant z \leqslant 0.125$. We also utilize $N_{\rm th} = 17$ for all members and $N_{\rm th} = 13$ for red members within R_{200}. We call these two subsamples $\mathcal{S}{\rm all}_{17}$ and $\mathcal{S}{\rm red}_{13}$. In Section 4.3, we investigate the systematics introduced by adopting $N_{\rm th}$.

3. The Mass–Richness Relation

In this section, we introduce our methodology for fitting the MRR, and then we apply it to the fiducial GalWCat19 subsamples $\mathcal{S}{\rm all}_{17}$ and $\mathcal{S}{\rm all}_{13}$ to derive the best-fit normalization α, slope β, and intrinsic scatter $\sigma_{\rm int}$ parameters.

3.1. Methodology of Fitting the Mass–Richness Relation

The probability distribution of the mass of haloes with a fixed richness N is given by a lognormal distribution (e.g., Saro et al. 2015; Simet et al. 2017; Chiu et al. 2020) as

$$P(\log M|N, z) = \frac{1}{\sqrt{2\pi\sigma^2_{\log M,N}}} \times \exp\left[-\frac{(\log M - \langle \log M|N\rangle)^2}{2\sigma^2_{\log M,N}}\right], \quad (5)$$

where the mean mass $\langle \log M|N\rangle$ is given as

$$\langle \log M|N\rangle = \alpha + \beta \log N, \quad (6)$$

In addition, the total variance in the mass $\sigma^2_{\log M,N}$ at a fixed richness, including contributions of the richness measurement errors $\sqrt{N}$, mass measurement errors $\sigma_{\log M}$, and the intrinsic scatter in mass $\sigma_{\rm int}$, is modeled by

$$\sigma^2_{\log M,N} = \frac{\beta^2}{N^2} + \sigma^2_{\log M} + \sigma^2_{\rm int}, \quad (7)$$

where α is the normalization and β is the slope of the mass–richness relation. Note that we ignore the evolution term in the MRR relation (Equation (6)) because our redshift range is very small ($0.045 \leqslant z \leqslant 0.0125$) and including this team does not affect our results. We estimate the model parameters α, β, and $\sigma_{\rm int}$ with the affine-invariant Markov chain Monte Carlo (MCMC) sampler of Goodman & Weare (2010) as implemented in the MATLAB package GWMCMC[11] inspired by the python package emcee (Foreman-Mackey et al. 2013).

Using MCMC fitting we now derive best-fit parameters for the MRR within R_{200}. For $\mathcal{S}{\rm all}_{17}$ we get $\alpha = 12.98 \pm 0.04$ $[h^{-1}\,M_\odot]$, $\beta = 0.96 \pm 0.03$, and $\sigma_{\rm int} = 0.12 \pm 0.01$. For $\mathcal{S}{\rm red}_{13}$ we obtain $\alpha = 13.08 \pm 0.03$ $[h^{-1}\,M_\odot]$, $\beta = 0.95 \pm 0.02$, and $\sigma_{\rm int} = 0.11 \pm 0.01$. In Section 4.3, we discuss the systematics of adopting the redshift, mass, and richness thresholds on our best-fit estimates of the MRR relation.

3.2. Comparison to Previous Results

Table 2 compares our best-fit parameters for the red MRR ($\rm MRR_{red}$) to those previously published by other groups who analyzed different cluster catalogs (see also Figure 3). We note that the normalization and slope of our MRR are noticeably different from other analyses. This is because we derived the MRR from the spectroscopic galaxy cluster catalog while other

[11] https://github.com/grinsted/gwmcmc

Table 2
Comparison of Best-fit Parameters for the MRR_{red} Derived Here with Previously Published Values Using Different Catalogs

References	Sample Membership	10^{α} $(10^{12}\ h^{-1}\ M_{\odot})$	β	Redshift
Johnston et al. (2007)	photo-SDSS-MaxBCG[a]	1.90 ± 0.26	1.28 ± 0.04	0.10–0.30
Simet et al. (2012)	photo-SDSS-MaxBCG	3.54 ± 0.28	1.10 ± 0.12	0.10–0.30
Oguri (2014)	photo-SDSS-CAMIRA[b]	1.25 ± 0.15	1.44 ± 0.27	0.10–0.60
Baxter et al. (2016)	photo-SDSS-redMaPPer[c]	4.84 ± 0.96	1.18 ± 0.16	0.18–0.33
Simet et al. (2017)	photo-SDSS-redMaPPer	1.64 ± 0.12	1.33 ± 0.09	0.10–0.33
Melchior et al. (2017)	photo-DES-redMaPPer[d]	3.55 ± 0.57	1.12 ± 0.20	0.20–0.80
Pereira et al. (2018)	photo-SDSS-redMaPPer[e]	3.17 ± 0.12	1.18 ± 0.09	0.10–0.33
Costanzi et al. (2019)	photo-SDSS-redMaPPer	2.42 ± 0.17	1.29 ± 0.09	0.10–0.30
This work ($\mathcal{S}\mathrm{red}_{13}$)	spec-SDSS-GalWCat19	11.4 ± 0.16	0.95 ± 0.02	0.045–0.125

Notes. All parameters have been calibrated to pivotal richness $N_{piv} = 1$.
[a] A red-sequence cluster finder (Koester et al. 2007).
[b] CAMIRA = Cluster finding algorithm based on Multi-band Identification of red galaxies.
[c] Baxter et al. (2016) used a subsample of the SDSS redMaPPer cluster catalog (Rykoff et al. 2014), which is in the North Galactic Cap (NGC). Here $\log(M_0)$ is calculated at $z = 0.089$ (mean redshift of GalWCat19).
[d] Melchior et al. (2017) used the DES (Dark Energy Survey) redMaPPer cluster catalog (Rykoff et al. 2016). Here $\log(M_0)$ is calculated at $z = 0.089$.
[e] Pereira et al. (2018) used 230 redMaPPer clusters obtained from Rykoff et al. (2016) and 136 VT clusters obtained from Wiesner et al. (2015)

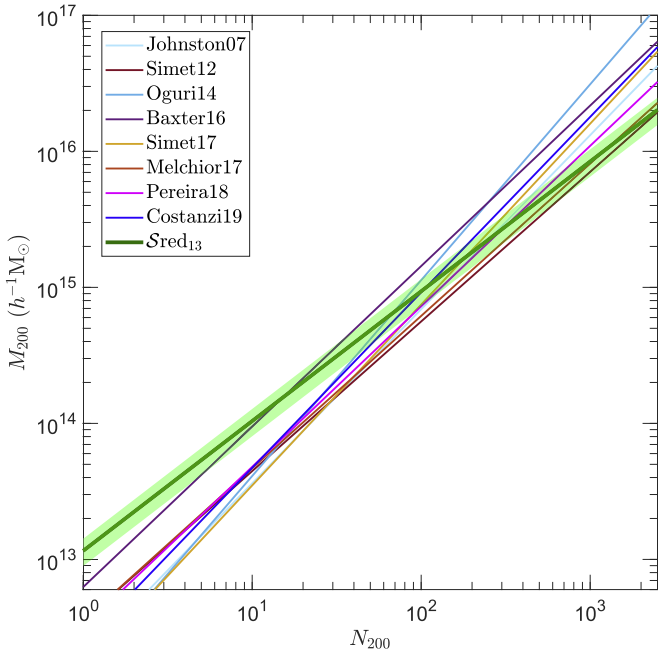

Figure 3. Comparison of the best-fit red MRR, MRR_{red}, derived in this work from $\mathcal{S}\mathrm{red}_{13}$ (dark green line with shading indicating 1σ uncertainty) with results reported in the literature (see legend and Table 2).

studies used photometric catalogs. As we discussed in the introduction, photometric catalogs have large systematical uncertainties because distances inferred from photometric redshift estimates are less accurate than those inferred from spectroscopic redshifts which increases the systematics of the projection effect. Moreover, cluster catalogs constructed from photometric surveys do not return an estimate of each cluster's mass directly. The masses of these clusters are calibrated via stacking clusters with the same richness and following up a subset of clusters with known masses that are calculated individually using different mass estimators such as weak lensing or X-ray observations (e.g., Simet et al. 2017).

Also, both the table and the figure demonstrate significant differences in the best-fit parameters among the different studies, even for those studies that analyzed the same catalogs, e.g., Johnston et al. (2007) and Simet et al. (2012) who utilized the SDSS-MaxBCG catalog of Koester et al. (2007), Baxter et al. (2016), Simet et al. (2017), and Costanzi et al. (2019) who utilized the SDSS redMaPPer catalog.

The tension in the MRR parameters obtained from different studies can be explained as follows. In deriving the MRR it is necessary to independently calculate the richness and the mass of each cluster. On the one hand, estimating cluster richness is complicated. It depends on the cluster-finder method, the projection effect, the completeness of the sample, the definition of the cluster richness, cluster evolution, and the aperture within which the richness is calculated. On the other hand, calculating cluster mass is also complicated. Cluster masses can be calculated by the virial mass estimator, weak gravitational lensing, and X-ray observations. However, these methods often return biased results owing to the assumption of hydrostatic equilibrium, projection effect, possible velocity anisotropies in galaxy orbits, the assumption that halo mass follows light (or stellar mass), the presence of substructure and/or nearby structure, the presence of interlopers in the cluster frame (see, e.g., Tonry & Davis 1981; The & White 1986; Fadda et al. 1996; Abdullah et al. 2013; Zhang et al. 2019).

In addition to the aforementioned factors, the size of the subsample used for the MRR calibration is usually small (tens of clusters), which introduces large uncertainties in both the slope and the normalization of the MRR relation. Moreover, many cluster catalogs span a large redshift range, so evolution (due to both the evolution of the universe and the physical processes of baryons in clusters) in the scaling relations used to estimate the masses needs to be carefully handled, introducing another source of uncertainty. Other observational systematics that introduce additional uncertainties are photometric redshift errors and cluster miscentering. All of the aforementioned factors can introduce significant uncertainties in the estimates of both the cluster richness and mass and consequently the constraints on MRR parameters (e.g., Henry et al. 2009; Mantz

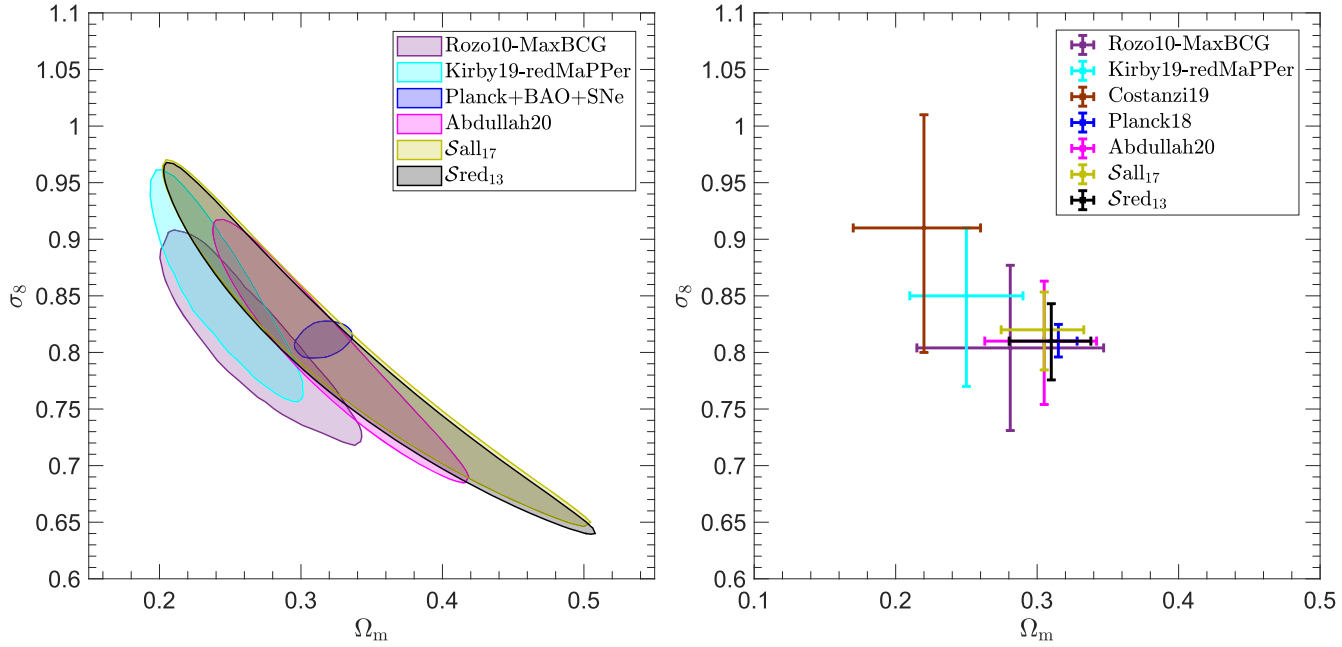

Figure 4. Comparison of constraints obtained on Ω_m and σ_8 in this work with those obtained from previous MRR analyses using different cluster catalogs and richness thresholds. Left: 68% CLs derived within R_{200} for all members with $N_{th} = 17$ (yellow, $\mathcal{S}$all$_{17}$) and red members with $N_{th} = 13$ (gray, $\mathcal{S}$all$_{13}$). Right: uncertainties on Ω_m and σ_8 estimated from the previous studies of Rozo et al. (2010), Costanzi et al. (2019), Kirby et al. (2019), and Lesci et al. (2022; purple, brown, cyan, respectively), which use the cluster abundance technique and cluster mass estimates from the mass–richness relation (CMF$_{MRR}$). Also shown is the study by Abdullah et al. (2020b; pink), which uses the cluster abundance technique and cluster mass estimates from the dynamics of member galaxies (CMF$_{dyn}$), and the study by Aghanim et al. (2020; blue), which uses the CMB technique (see Table 1 for the abbreviation).

et al. 2015) and Ω_m and σ_8 parameters as well (see Section 4.1 and Figure 4).

4. Implications for Cosmological Models and Constraining Ω_m and σ_8

In this section, we summarize our procedure for constraining Ω_m and σ_8. We start with calculating the halo (cluster) mass function (HMF) from theory, comparing it with the CMF we obtain from the MRR relation, and then constraining Ω_m and σ_8. Full details can be found in Abdullah et al. (2020a).

4.1. Prediction of the HMF

The number of clusters per unit mass per unit comoving volume of the universe is given by

$$\frac{dn}{d\ln M} = f(\sigma)\frac{\rho_0}{M}\left|\frac{d\ln\sigma}{d\ln M}\right|, \quad (8)$$

where ρ_0 is the mean density of the universe, σ is the rms mass variance on a scale of radius R that contains a mass $M = 4\pi\rho_0 R^3/3$, and $f(\sigma)$ represents the functional form that defines a particular HMF fit. We adopt the functional form of Tinker et al. (2008; hereafter Tinker08) to calculate the HMF and consequently the predicted abundance of clusters. The Tinker08 function is given by

$$f(\sigma, z) = A\left[\left(\frac{\sigma}{b}\right)^{-a} + 1\right]\exp(-c/\sigma^2), \quad (9)$$

where $A = 0.186(1+z)^{-0.14}$, $a = 1.47(1+z)^{-0.06}$, $b = 2.57(1+z)^{-\alpha}$, $c = 1.19$, and $\ln\alpha(\Delta_{vir}) = [75/(\ln(\Delta_{vir}/75))]^{1.2}$, and σ^2 is the mass variance defined as

$$\sigma^2(M, z) = \frac{g(z)}{2\pi}\int P(k)W^2(kR)k^2dk. \quad (10)$$

$P(k)$ is the current linear matter power spectrum (at $z = 0$) as a function of wavenumber k, $W(kR) = 3[\sin(kR) - kR\cos(kR)])/(kR)^3$ is the Fourier transform of the real-space top-hat window function of radius R, and $g(z) = \sigma_8(z)/\sigma_8(0)$ is the growth factor of linear perturbations at scales of $8h^{-1}$ Mpc, normalized to unity at $z = 0$. For more details regarding the calculation of the HMF, we refer the reader to, e.g., Press & Schechter (1974), Tinker & Wetzel (2010), Behroozi et al. (2013a), and Shirasaki et al. (2021).

We calculate the predicted HMF by allowing Ω_m to vary between [0.1, 0.6] and σ_8 between [0.6, 1.2], in both cases in steps of 0.005. We keep the following cosmological parameters fixed: the CMB temperature $T_{cmb} = 2.725$ K, baryonic density $\Omega_b = 0.0486$, and spectral index $n = 0.967$ (Ade et al. 2014), at redshift $z = 0.089$ (the mean redshift of `GalWCat19`).

In order to calculate the CMF from observation we begin by deriving MRR relations for both the $\mathcal{S}$all$_{17}$ and $\mathcal{S}$red$_{13}$ subsamples. We then estimate the mass of each cluster knowing its richness and calculate the CMF from observations. The CMF is calculated for clusters with masses $\log M_{200} \geqslant 13.9$ $[h^{-1}M_\odot]$ and in the redshift range of $0.045 \leqslant z \leqslant 0.125$. Abdullah et al. (2020b) showed that, for clusters in the redshift range of $0.045 \leqslant z \leqslant 0.125$, the effect of evolution on the HMF is less than 3%. Note that in this work, rather than utilizing the dynamically derived estimate of cluster mass in `GalWCat19`, we reestimate each cluster mass from its richness using the best-fit MRR and calculate the CMF from those masses.

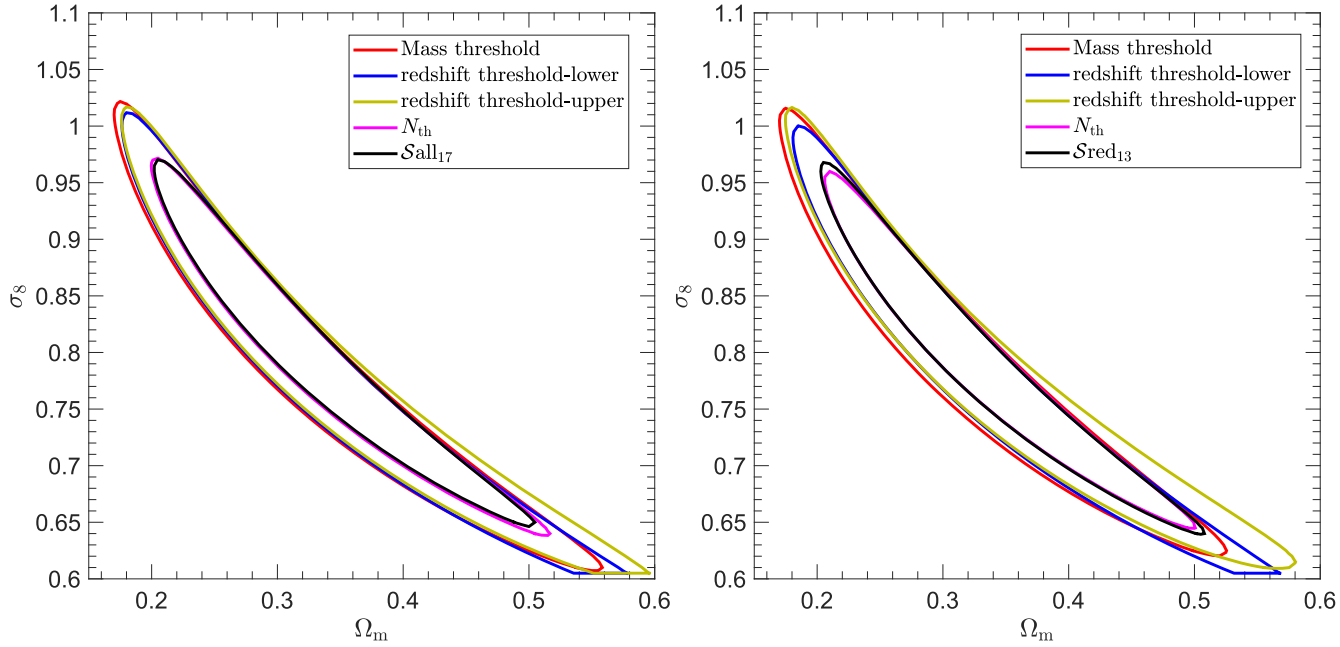

Figure 5. Systematical effects of cluster mass, lower and upper redshifts, and richness thresholds on our constraints on the cosmological parameters for the analysis on the fiducial samples of $\mathcal{S}{\rm all}_{17}$ for all members within R_{200} (left) and $\mathcal{S}{\rm red}_{13}$ for red members within R_{200} (right; see Section 4.3 for details). The 68% CLs for our fiducial sample, varying mass threshold $\log M_{200}$ between 13.8 and 14.0 $[h^{-1}\,M_{\odot}]$, fixing the upper redshift threshold to 0.125 and varying the lower redshift threshold from 0.01 to 0.07, fixing the lower redshift threshold to 0.045 and varying the upper redshift threshold from 0.11 to 0.15, varying $N_{\rm th}$ from 15 to 19 for $\mathcal{S}{\rm all}_{17}$, and varying $N_{\rm th}$ from 13 to 17 for $\mathcal{S}{\rm red}_{13}$.

Finally, in order to determine the best-fit mass function and constrain $\Omega_{\rm m}$ and σ_8 we use a standard χ^2 procedure

$$\chi^2 = \sum_{i=1}^{N}\left(\frac{[y_{o,i} - y_{m,i}]^2}{\sigma_i^2}\right), \tag{11}$$

where the likelihood, $\mathcal{L}(y|\sigma_8, \Omega_{\rm m})$, of a data point y_o given a model y_m is

$$\mathcal{L}(y|\sigma_8, \Omega_{\rm m}) \propto \exp\left(\frac{-\chi^2(y|\sigma_8, \Omega_{\rm m})}{2}\right). \tag{12}$$

Note that σ includes the statistical uncertainty of the data plus the intrinsic scatter $\sigma_{\rm int}$ obtained from the MRR relation (Equation (7)).

4.2. Constraints on the Cosmological Parameters Ω_m and σ_8

In this section, we present the constraints we obtained on $\Omega_{\rm m}$ and σ_8 by first using the MRR derived from all members ($\mathcal{S}{\rm all}_{17}$) and then from red members ($\mathcal{S}{\rm red}_{13}$). We also compare the constraints we derive first to the cosmological constraints obtained from other groups who fit to MRR relations, and then to the cosmological constraints obtained from Aghanim et al. (2020) who utilized the CMB technique.

As discussed in Section 4.1, we derive the cosmological parameters $\Omega_{\rm m}$ and σ_8, after estimating each cluster mass in either the full or red subsample using its MRR. Utilizing the subsample of clusters with all members, $\mathcal{S}{\rm all}_{17}$, we obtain $\Omega_{\rm m} = 0.31^{+0.03}_{-0.03}$ and $\sigma_8 = 0.82^{+0.03}_{-0.04}$. Utilizing the subsample of clusters with red members, $\mathcal{S}{\rm red}_{13}$, we find $\Omega_{\rm m} = 0.31^{+0.03}_{-0.03}$ and $\sigma_8 = 0.81^{+0.03}_{-0.03}$. Figure 4 shows our constraints on $\Omega_{\rm m}$ and σ_8 using the subsamples $\mathcal{S}{\rm all}_{17}$ and $\mathcal{S}{\rm red}_{13}$, as well as previously published constraints from Rozo et al. (2010), Costanzi et al. (2019), Kirby et al. (2019), and Abdullah et al. (2020b), which use the MRR ($\rm CMF_{MRR}$) or dynamical ($\rm CMF_{dyn}$) cluster abundance techniques and Aghanim et al. (2020), which use the CMB technique (see Table 1 for more details). As shown in the figure, the 68% confidence levels (CLs) obtained from our catalogs $\mathcal{S}{\rm all}_{17}$ (yellow) and $\mathcal{S}{\rm red}_{13}$ (gray) are very consistent and overlap with each other. Our 68% CLs are also consistent with the 68% CLs obtained by the other groups. However, despite this overlapping, the right panel of Figure 4 shows that the constraints on $\Omega_{\rm m}$ and σ_8 obtained from the $\rm CMF_{MRR}$ techniques are in tension with each other. This tension comes from the discrepancy between the MRRs derived by the different studies as discussed in Section 2.2. We end by noting that the constraints we derive on $\Omega_{\rm m}$ and σ_8 here from the MRR agree very well both with the constraints derived by Aghanim et al. (2020) and Abdullah et al. (2020b) using the two independent techniques of CMB and cluster dynamics, respectively (although this work and Abdullah et al. 2020b did utilize the same SDSS catalog). In Section 4.3, we discuss the systematics on the cosmological constraints introduced by adopting redshift, mass, and richness thresholds.

4.3. Systematics

In this section, we discuss the systematics introduced when deriving the MRR and cosmological parameters due to the adoption of the cluster mass threshold $\log M_{200} \geqslant 13.9$ $[h^{-1}\,M_{\odot}]$, the lower and upper redshift thresholds $0.045 \leqslant z \leqslant 0.125$, and the richness thresholds $N_{\rm th} = 17$ for $\mathcal{S}{\rm all}_{17}$ and $N_{\rm th} = 13$ for $\mathcal{S}{\rm red}_{13}$.

The first systematic uncertainty comes from the difficulty of accurately determining the mass threshold at which the sample is mass complete. As discussed in Section 2.2 the catalog is approximately complete around $\log M_{200} \gtrsim 13.9$ $[h^{-1}\,M_{\odot}]$. We investigate the effect of varying the mass threshold $\log M_{200}$

Table 3
Dependence of MRR and Cosmological Parameters on Mass, Lower and Upper Redshifts, and Richness Thresholds (Section 4.3)

	Sample	Threshold Range	α	β	Ω_m	σ_8
Mass threshold	All	$\log M_{200,th} = [13.8–14.0]$	12.97 ± 0.10	0.96 ± 0.06	0.30 ± 0.03	0.82 ± 0.02
Mass threshold	Red	$\log M_{200,th} = [13.8–14.0]$	13.06 ± 0.10	0.96 ± 0.06	0.30 ± 0.02	0.81 ± 0.03
Redshift lower threshold	All	$z_{th} = [0.01–0.07]$	12.97 ± 0.01	0.96 ± 0.01	0.31 ± 0.01	0.81 ± 0.02
Redshift lower threshold	Red	$z_{th} = [0.01–0.07]$	13.07 ± 0.01	0.95 ± 0.01	0.31 ± 0.01	0.81 ± 0.01
Redshift upper threshold	All	$z_{th} = [0.10–0.15]$	13.01 ± 0.11	0.93 ± 0.05	0.33 ± 0.05	0.80 ± 0.07
Redshift upper threshold	Red	$z_{th} = [0.10–0.15]$	13.13 ± 0.13	0.91 ± 0.07	0.34 ± 0.09	0.80 ± 0.08
Richness threshold	All	$N_{th} = [15–19]$	12.98 ± 0.10	0.96 ± 0.06	0.31 ± 0.03	0.82 ± 0.04
Richness threshold	Red	$N_{th} = [11–15]$	13.10 ± 0.10	0.94 ± 0.05	0.32 ± 0.03	0.81 ± 0.03

between 13.8 and 14.0 $[h^{-1} M_\odot]$ on the derived MRR and cosmological parameters from our analysis. For each mass threshold, we calculate the χ^2 likelihood and then we obtain the joint 68% CL of all χ distributions as shown in Figure 5. The systematic uncertainties in MRR and cosmological parameters are listed in Table 3. Both the plot and the table show that the best-fit value of each parameter deviates only very slightly from the results of the fiducial samples $\mathcal{S}\mathrm{all}_{17}$ and $\mathcal{S}\mathrm{red}_{13}$.

The second systematic uncertainty comes from the choice of the redshift interval. We first fix the upper redshift threshold to $z = 0.125$ and vary the lower redshift threshold from 0.01 to 0.07. Both Figure 5 and Table 3 indicate that varying the lower redshift threshold does not affect our result for the fiducial samples $\mathcal{S}\mathrm{all}_{17}$ and $\mathcal{S}\mathrm{red}_{13}$. It demonstrates that the evolution effect is unremarkable in this small redshift interval (see also Abdullah et al. 2020b). We then fix the lower redshift threshold to $z = 0.045$ and vary the upper redshift threshold from 0.10 to 0.15. The best-fit value of each parameter deviates slightly from the results of the fiducial samples $\mathcal{S}\mathrm{all}_{17}$ and $\mathcal{S}\mathrm{red}_{13}$.

The third systematic uncertainty comes from the choice of the richness threshold N_{th}. Therefore, we investigate the effect of varying N_{th} between 15 and 19 for $\mathcal{S}\mathrm{all}_{17}$ and N_{th} between 13 and 17 for $\mathcal{S}\mathrm{red}_{13}$ on the derived MRR and cosmological parameters. Both Figure 5 and Table 3 show that the best-fit value of each parameter deviates very slightly from the results of the fiducial samples $\mathcal{S}\mathrm{all}_{17}$ and $\mathcal{S}\mathrm{red}_{13}$.

5. Conclusions

In this paper, we utilized the `GalWCat19`cluster catalog (Abdullah et al. 2020b), constructed from the SDSS-DR13 spectroscopic data set, to derive the MRR and constrain Ω_m and σ_8.

1. The MRR was observed to show a tail at the low-richness end. Using the IllustrisTNG and mini-Uchuu cosmological numerical simulations, we demonstrated that this tail was not intrinsic. Furthermore, we presented a technique to identify the optimal richness threshold, (N_{th}), below which clusters should be discarded prior to deriving the MRR. This threshold is dependent on the cluster catalog being utilized. We showed how to apply a Hinge function to optimally determine N_{th} appropriate for any catalog. Using this method, we derived an optimal threshold of $N_{th} = 17\,(13)$ for all (red) member galaxies in the `GalWCat19` catalog.
2. Using MCMC fitting (Section 3.1) we derived the best-fit parameters for the MRR within R_{200} (Section 3). For $\mathcal{S}\mathrm{all}_{17}$ we obtained $\alpha = 12.98 \pm 0.04$ $[h^{-1} M_\odot]$, $\beta = 0.96 \pm 0.03$, and $\sigma_{int} = 0.12 \pm 0.01$. For $\mathcal{S}\mathrm{red}_{13}$ we obtained $\alpha = 13.08 \pm 0.03$ $[h^{-1} M_\odot]$, $\beta = 0.95 \pm 0.02$, and $\sigma_{int} = 0.11 \pm 0.01$.
3. The slope of the MRR we derived was consistent with both the IllustrisTNG and mini-Uchuu numerical simulations while MRRs in the literature that were derived from photometric catalogs obtained a steeper slope. This is likely because we derived our MRR using a spectroscopic galaxy cluster catalog while previously published analyses used photometric catalogs.
4. We (re-)estimated the mass of each cluster in the `GalWCat19` catalog using the MRR relation. We then derived constraints on Ω_m and σ_8 using the cluster abundance technique (Sections 4.1 and 3.1). Using the MRR determined from all members, $\mathcal{S}\mathrm{all}_{17}$, we obtained $\Omega_m = 0.31^{+0.03}_{-0.03}$ and $\sigma_8 = 0.82^{+0.03}_{-0.04}$. For red members, $\mathcal{S}\mathrm{red}_{13}$, we obtained $\Omega_m = 0.31^{+0.03}_{-0.03}$ and $\sigma_8 = 0.81^{+0.03}_{-0.03}$. We compared our results to those from Rozo et al. (2010), Costanzi et al. (2019), Kirby et al. (2019), and Lesci et al. (2022), works that also used cluster abundance and the MRR technique to derive cluster masses ($\mathrm{CMF}_{\mathrm{MRR}}$). We also compared our results to those of Abdullah et al. (2020b), which used cluster abundances but the galaxy dynamics technique to derive cluster masses ($\mathrm{CMF}_{\mathrm{dyn}}$) and with Aghanim et al. (2020) who used the CMB rather than the cluster abundance technique (see Table 1 for an explanation of the abbreviations). We found that the constraints we derived using the full ($\mathcal{S}\mathrm{all}_{17}$) and red galaxy ($\mathcal{S}\mathrm{red}_{13}$) MRRs were consistent with each other. Reassuringly, the constraints we obtained on Ω_m and σ_8 were also consistent with those obtained both by Aghanim et al. (2020) and Abdullah et al. (2020b), which were determined using independent techniques to those utilized here.
5. We investigated the systematics introduced by adopting mass, redshift, and richness thresholds when deriving the MRR and cosmological parameters (Section 4.3). We found that the best-fit value of each parameter deviated only slightly from those of the two fiducial samples of $\mathcal{S}\mathrm{all}_{17}$ and $\mathcal{S}\mathrm{red}_{13}$ (Figure 4 and Table 3).

In conclusion, we demonstrated that the MRR is a powerful and effective tool for constraining cosmological constraints using the cluster abundance technique.

Acknowledgments

We appreciate the comments and suggestions of the reviewer, which improved this paper. We gratefully acknowledge support from the Japan Society for the Promotion of Science through JSPS KAKENHI grant No. JP21F51024. We

gratefully acknowledge support from the National Science Foundation through grant AST-2205189, and from HST program Nos. GO-15294 and GO-16300. Support for program Nos. GO-15294 and GO-16300 was provided by NASA through grants from the Space Telescope Science Institute, which is operated by the Association of Universities for Research in Astronomy, Incorporated, under NASA contract NAS5-26555. T.I. has been supported by IAAR Research Support Program at Chiba University Japan, MEXT/JSPS KAKENHI (grant Nos. JP19KK0344 and JP21H01122), MEXT as "Program for Promoting Research on the Supercomputer Fugaku" (JPMXP1020200109), and JICFuS. We thank Instituto de Astrofísica de Andalucía (IAA-CSIC), Centro de Supercomputación de Galicia (CESGA), and the Spanish academic and research network (RedIRIS) in Spain for hosting Uchuu Data Release 1 in the Skies & Universes site for cosmological simulations. The Uchuu simulations were carried out on the Aterui II supercomputer at the Center for Computational Astrophysics, CfCA, of the National Astronomical Observatory of Japan, and the K computer at the RIKEN Advanced Institute for Computational Science. The Uchuu DR1 effort has made use of the skun@IAA_RedIRIS and skun6@IAA computer facilities managed by the IAA-CSIC in Spain (MICINN EU-Feder grant EQC2018-004366-P).

Appendix A
Separating Red and Blue Galaxies

In this section, we describe our procedure to identify the red-sequence galaxies of `GalWCat19` members. It is well known that clusters are dominated by elliptical, red E/S0 galaxies which occupy a narrow region in the CMD known as the E/S0 ridgeline or red sequence (e.g., Baum 1959; Bower et al. 1992; Gladders & Yee 2000). The location and the slope of this ridgeline in color decrease smoothly with increasing redshift (Koester et al. 2007) which is mainly attributed to a k-correction effect (e.g., Kodama & Arimoto 1997; López-Cruz et al. 2004). The `GalWCat19` catalog contains clusters in the redshift range of $0.01 \leqslant z \leqslant 0.2$. In order to identify red members, we sort the clusters into 14 equally sized redshift bins, each approximately spanning $\Delta z = 0.01$. Then, for each redshift bin, we plot the members in the rest-frame $g - r$ versus M_r CMD to identify the ridgeline. The ridgeline is defined to be the line with maximum likelihood (or pdf) in color for the distribution of galaxies in the CMD (see the first two nested panels in Figure A1). This ridgeline can be located using the two-dimensional adaptive kernel method (2DAKM, see e.g., Pisani 1996) or the Gaussian mixture model for red-sequence galaxy identification (Hao et al. 2009). In this paper, we apply the 2DAKM to identify the location of the ridgeline. We then locate the line with a probability of 1σ CL below the ridgeline. We define red galaxies as those with rest-frame color above the 1σ line.

Figure A1 shows the CMD of `GalWCat19` galaxies at two redshift bins $0.05 \leqslant z \leqslant 0.06$ and $0.08 \leqslant z \leqslant 0.09$. The solid cyan line in each panel represents the red-sequence ridgeline and the dashed line is the line that separates the red and blue galaxies with the probability of 1σ CL from the ridgeline. In the right panel of Figure A1, we plot the color–redshift relation. The plot demonstrates that the slope of the ridgeline varies with redshift.

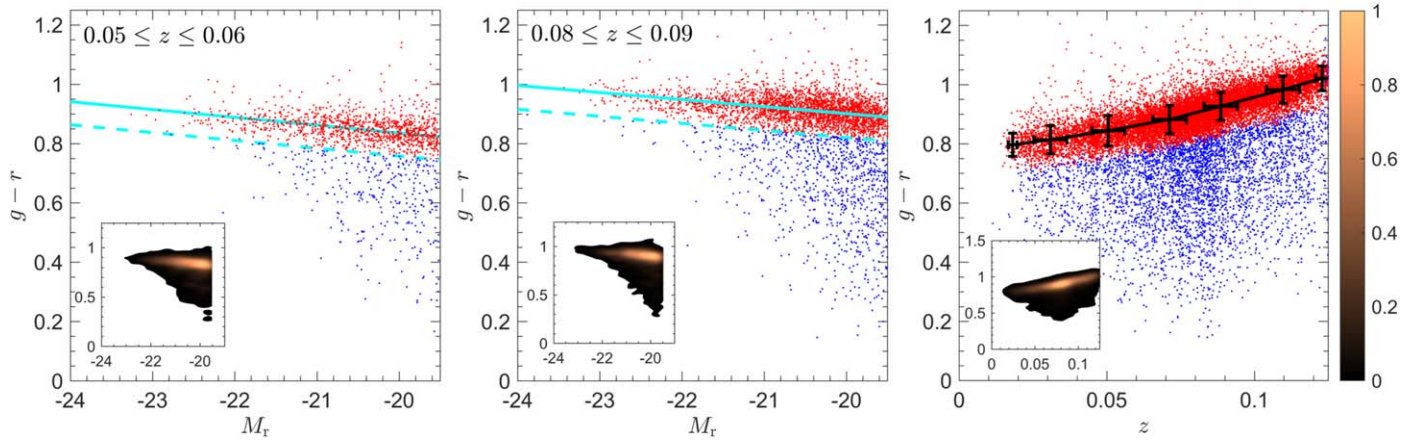

Figure A1. Separating red and blue members of the `GalWCat19` clusters using the CMD. The left and middle panels show the CMD for cluster members in two different redshift bins. The solid cyan line in each panel shows the red-sequence ridgeline (highest probability) and the dashed line is the line that separates red and blue members at the 1σ CL from the ridgeline. The right panel shows the evolution of the ridgeline as a function redshift. The black line shows the mean color of the red members as a function of redshift with 1σ uncertainties. The nested panels show the probability distribution functions for galaxies in the CMD.

Appendix B
Is the MRR Tail Intrinsic?

In Figure B1, we plot the MRR relation for the mini-Uchuu and IllustrisTNG simulations. For the mini-Uchuu simulations, we plot MRR for five $v_{\rm peak}$ thresholds for subhaloes, and for the IllustrisTNG haloes we present MRR for four M_s thresholds for galaxies both within r_{200}. The figure shows a short tail at the low-richness end. The tail increases with increasing the thresholds of $v_{\rm peak}$ for mini-Uchuu and M_s for TNG of the selected sample from each simulation. We conclude that this tail is not intrinsic and the effect at low richness is partially due to the threshold of simulations as well as Poisson scattering.

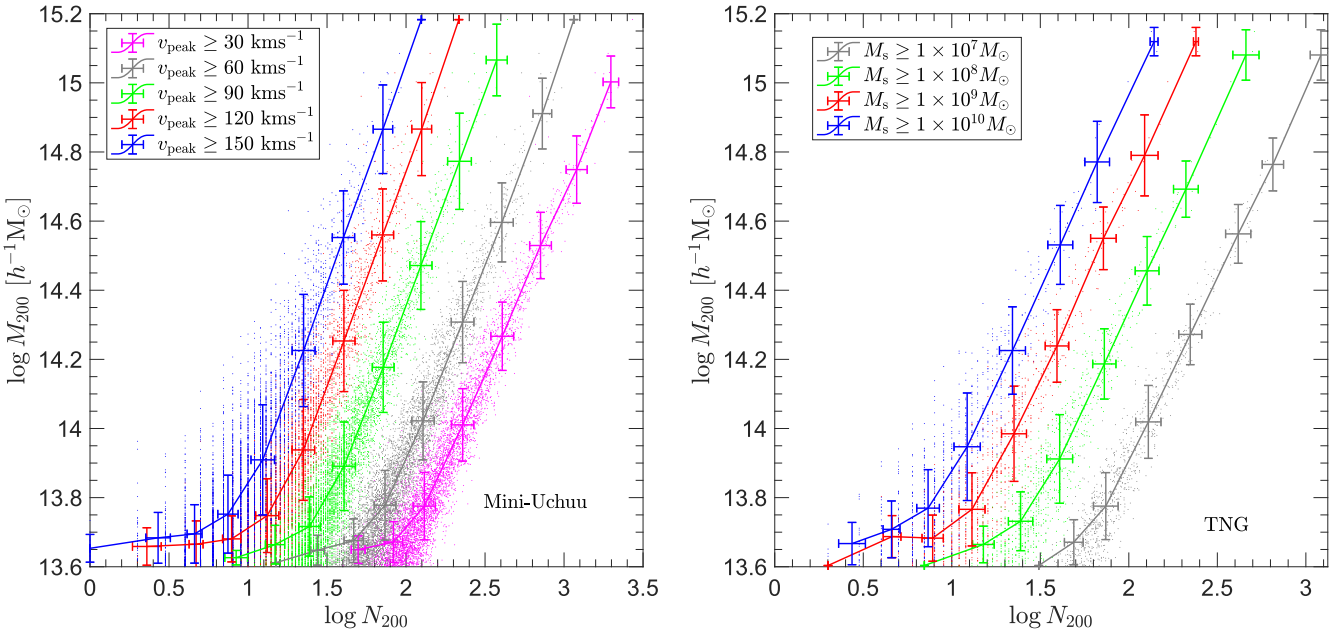

Figure B1. MRR for simulations. The mean mass at some richness bins is plotted for mini-Uchuu (left) for five $v_{\rm peak}$ thresholds for subhaloes and TNG (right) for four M_s thresholds for galaxies within r_{200} as shown in each legend. Error bars represent Poisson noise. The figure shows that MRR introduces a tail at the low-richness end. The length of the tail increases with the increases in the thresholds of $v_{\rm peak}$ and M_s. This indicates that the tail is dependent on the selection of the threshold and it is not intrinsic.

Appendix C
Optimal Richness Threshold

In this section, we discuss the effect of the choice of optimal richness threshold on the derivation of the MRR relation. Figure C1 shows the best-fit MRRs as a function of the choice of richness threshold for all (left) and red (right) members. The figure shows that, for both $\mathrm{MRR_{all}}$ and $\mathrm{MRR_{red}}$, the normalization (α) decreases and the slope (β) increases rapidly from $N_{\rm th} = 9$ to the optimal richness threshold $N_{\rm th} = 17$, and then flattens for higher richness thresholds. In other words, α and β vary significantly for $N_{\rm th} \lesssim 17$ ($N_{\rm th} \lesssim 13$) for $\mathrm{MRR_{all}}$ ($\mathrm{MRR_{red}}$) while they vary only slightly for $N_{\rm th} \gtrsim 17$ ($N_{\rm th} \gtrsim 13$) for $\mathrm{MRR_{all}}$ ($\mathrm{MRR_{red}}$). The significant variation in the best-fit MRR parameters determined when a richness threshold smaller than the optimal value is adopted, is due to the effect of the tail artifact discussed in Section 2.3. The slight change ($\lesssim$5%) in the best-fit MRR parameters for large richness thresholds is because applying a higher richness threshold decreases the number of clusters available to be used in the fit (i.e., due to Poisson noise).

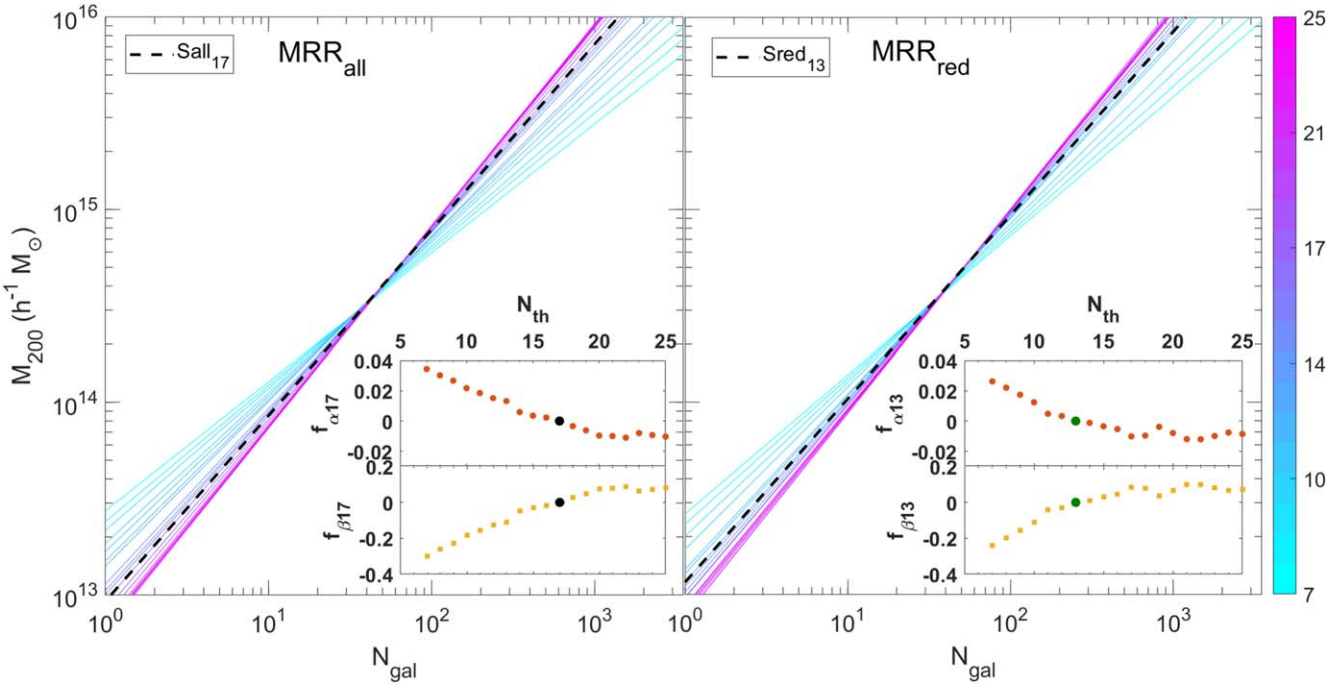

Figure C1. Best-fit MRRs for all (left) and red (right) cluster members within R_{200}. Colored lines illustrate how the best-fit MRRs vary as a function of the choice of richness threshold parameter, with values ranging from $N_{\rm th} = 7$ (cyan) to $N_{\rm th} = 25$ (magenta). The black (dark green) dashed line shows the MRR for the fiducial subsample of the threshold parameter in each case, i.e., $\mathcal{S}\mathrm{all}_{17}$ for all members ($\mathcal{S}\mathrm{red}_{13}$ for red members) with $N_{\rm th} = 17$ ($N_{\rm th} = 13$). The upper nested panel on the left shows the scatter $f_{\alpha 17} = (\alpha_{N_{\rm th}} - \alpha_{N_{17}})/\alpha_{N_{17}}$ and the lower nested left shows $f_{\beta 17} = (\beta_{N_{\rm th}} - \beta_{N_{17}})/\beta_{N_{17}}$ relative to $\alpha_{N_{17}}$ and $\beta_{N_{17}}$ (black points), respectively. Nested right panels are the same as the left nested panels but relative to $\alpha_{N_{13}}$ and $\beta_{N_{13}}$ (green points) for $N_{\rm th} = 13$. See Appendix C for a discussion.

ORCID iDs

Mohamed H. Abdullah https://orcid.org/0000-0003-3595-7147
Gillian Wilson https://orcid.org/0000-0002-9513-8437
Tomoaki Ishiyama https://orcid.org/0000-0002-5316-9171

References

Abbott, T., Aguena, M., (DES Collaboration), et al. 2020, PhRvD, 102, 023509
Abbott, T. M. C., Abdalla, F. B., Allam, S., et al. 2018, ApJS, 239, 18
Abdullah, M. H., Klypin, A., & Wilson, G. 2020a, ApJ, 901, 90
Abdullah, M. H., Praton, E. A., & Ali, G. B. 2013, MNRAS, 434, 1989
Abdullah, M. H., Wilson, G., & Klypin, A. 2018, ApJ, 861, 22
Abdullah, M. H., Wilson, G., Klypin, A., et al. 2020b, ApJS, 246, 2
Abell, P. A., Allison, J., (LSST Science Collaboration), et al. 2009, arXiv:0912.0201
Adam, R., Vannier, M., (Euclid Collaboration), et al. 2019, A&A, 627, A23
Ade, P. A. R., Aghanim, N., (Planck Collaboration), et al. 2014, A&A, 571, A1
Ade, P. A. R., Aghanim, N., (Planck Collaboration), et al. 2016, A&A, 594, A13
Aghanim, N., Akrami, Y., (Planck Collaboration), et al. 2020, A&A, 641, A6
Akeson, R., Armus, L., Bachelet, E., et al. 2019, arXiv:1902.05569
Baes, M., & Camps, P. 2021, MNRAS, 503, 2955
Battye, R. A., & Weller, J. 2003, PhRvD, 68, 083506
Baum, W. A. 1959, PASP, 71, 106
Baxter, E. J., Rozo, E., Jain, B., Rykoff, E., & Wechsler, R. H. 2016, MNRAS, 463, 205
Behroozi, P. S., Wechsler, R. H., & Wu, H.-Y. 2013a, ApJ, 762, 109
Behroozi, P. S., Wechsler, R. H., Wu, H.-Y., et al. 2013b, ApJ, 763, 18
Beuermann, K., Hessman, F. V., Reinsch, K., et al. 1999, A&A, 352, L26
Binney, J., & Tremaine, S. 1987, Galactic Dynamics (Princeton, NJ: Princeton Univ. Press)
Biviano, A., Murante, G., Borgani, S., et al. 2006, A&A, 456, 23
Blanton, M. R., Hogg, D. W., Bahcall, N. A., et al. 2003, ApJ, 592, 819
Blanton, M. R., & Roweis, S. 2007, AJ, 133, 734
Bocquet, S., Saro, A., Mohr, J. J., et al. 2015, ApJ, 799, 214
Bower, R. G., Lucey, J. R., & Ellis, R. S. 1992, MNRAS, 254, 589
Carlberg, R. G., Yee, H. K. C., & Ellingson, E. 1997, ApJ, 478, 462
Chiu, I. N., Umetsu, K., Murata, R., Medezinski, E., & Oguri, M. 2020, MNRAS, 495, 428
Costanzi, M., Rozo, E., Simet, M., et al. 2019, MNRAS, 488, 4779
Dahle, H. 2006, ApJ, 653, 954
Deason, A. J., Belokurov, V., & Sanders, J. L. 2019, MNRAS, 490, 3426
Doré, O., Bock, J., Ashby, M., et al. 2014, arXiv:1412.4872
Fadda, D., Girardi, M., Giuricin, G., Mardirossian, F., & Mezzetti, M. 1996, ApJ, 473, 670
Foreman-Mackey, D., Hogg, D. W., Lang, D., & Goodman, J. 2013, PASP, 125, 306
Giuricin, G., Mardirossian, F., & Mezzetti, M. 1982, ApJ, 255, 361
Gladders, M. D., & Yee, H. K. C. 2000, AJ, 120, 2148
Goodman, J., & Weare, J. 2010, CAMCS, 5, 65
Hao, J., Koester, B. P., Mckay, T. A., et al. 2009, ApJ, 702, 745
Henry, J. P., Evrard, A. E., Hoekstra, H., Babul, A., & Mahdavi, A. 2009, ApJ, 691, 1307
Ishiyama, T., Fukushige, T., & Makino, J. 2009, PASJ, 61, 1319
Ishiyama, T., Nitadori, K., & Makino, J. 2012, arXiv:1211.4406
Ishiyama, T., Prada, F., Klypin, A. A., et al. 2021, MNRAS, 506, 4210
Jackson, J. C. 1972, MNRAS, 156, 1P
Johnston, D. E., Sheldon, E. S., Wechsler, R. H., et al. 2007, arXiv:0709.1159
Kaiser, N. 1987, MNRAS, 227, 1
Kauffmann, G., Colberg, J. M., Diaferio, A., & White, S. D. M. 1999, MNRAS, 303, 188
Kauffmann, G., Heckman, T. M., White, S. D. M., et al. 2003, MNRAS, 341, 33
Kirby, M., Rozo, E., Morris, R. G., et al. 2019, arXiv:1910.13548
Klypin, A., Yepes, G., Gottlöber, S., Prada, F., & Heß, S. 2016, MNRAS, 457, 4340
Kodama, T., & Arimoto, N. 1997, A&A, 320, 41
Koester, B. P., McKay, T. A., Annis, J., et al. 2007, ApJ, 660, 239
Lesci, G. F., Marulli, F., Moscardini, L., et al. 2022, A&A, 659, A88
Levi, M., Allen, L. E., Raichoor, A., et al. 2019, BAAS, 51, 57
López-Cruz, O., Barkhouse, W. A., & Yee, H. K. C. 2004, ApJ, 614, 679
Mantz, A. B., Allen, S. W., Morris, R. G., et al. 2016, MNRAS, 463, 3582
Mantz, A. B., von der Linden, A., Allen, S. W., et al. 2015, MNRAS, 446, 2205
Melchior, P., Gruen, D., McClintock, T., et al. 2017, MNRAS, 469, 4899
Merloni, A., Predehl, P., Becker, W., et al. 2012, arXiv:1209.3114
Merritt, D. 1988, in ASP Conf. Ser. 5, The Minnesota lectures on Clusters of Galaxies and Large-Scale Structure, ed. J. M. Dickey (San Francisco, CA: ASP), 175
Mowla, L., van der Wel, A., van Dokkum, P., & Miller, T. B. 2019, ApJL, 872, L13
Murata, R., Oguri, M., Nishimichi, T., et al. 2019, PASJ, 71, 107
Nelson, D., Springel, V., Pillepich, A., et al. 2019, ComAC, 6, 2
Oguri, M. 2014, MNRAS, 444, 147
Old, L., Wojtak, R., Mamon, G. A., et al. 2015, MNRAS, 449, 1897
Pereira, M. E. S., Soares-Santos, M., Makler, M., et al. 2018, MNRAS, 474, 1361
Pillepich, A., Springel, V., Nelson, D., et al. 2018, MNRAS, 473, 4077
Pisani, A. 1996, MNRAS, 278, 697
Pratt, G. W., Croston, J. H., Arnaud, M., & Böhringer, H. 2009, A&A, 498, 361
Press, W. H., & Schechter, P. 1974, ApJ, 187, 425
Rozo, E., Wechsler, R. H., Rykoff, E. S., et al. 2010, ApJ, 708, 645
Rykoff, E. S., Rozo, E., Busha, M. T., et al. 2014, ApJ, 785, 104
Rykoff, E. S., Rozo, E., Hollowood, D., et al. 2016, ApJS, 224, 1
Saro, A., Bocquet, S., Rozo, E., et al. 2015, MNRAS, 454, 2305
Serra, A. L., Diaferio, A., Murante, G., & Borgani, S. 2011, MNRAS, 412, 800
Shirasaki, M., Ishiyama, T., & Ando, S. 2021, ApJ, 922, 89
Simet, M., Kubo, J. M., Dodelson, S., et al. 2012, ApJ, 748, 128
Simet, M., McClintock, T., Mandelbaum, R., et al. 2017, MNRAS, 466, 3103
Springel, V. 2010, MNRAS, 401, 791
Takada, M., Ellis, R. S., Chiba, M., et al. 2014, PASJ, 66, R1
Tempel, E., Tamm, A., Gramann, M., et al. 2014, A&A, 566, A1
The, L. S., & White, S. D. M. 1986, AJ, 92, 1248
Tinker, J., Kravtsov, A. V., Klypin, A., et al. 2008, ApJ, 688, 709
Tinker, J. L., & Wetzel, A. R. 2010, ApJ, 719, 88
Tonry, J. L., & Davis, M. 1981, ApJ, 246, 680
Vikhlinin, A., Burenin, R. A., Ebeling, H., et al. 2009, ApJ, 692, 1033
Wang, L., & Steinhardt, P. J. 1998, ApJ, 508, 483
Weinberg, D. H., Mortonson, M. J., Eisenstein, D. J., et al. 2013, PhR, 530, 87
Weinberger, R., Springel, V., & Pakmor, R. 2020, ApJS, 248, 32
Wen, Z. L., Han, J. L., & Liu, F. S. 2010, MNRAS, 407, 533
White, S. D. M., & Frenk, C. S. 1991, ApJ, 379, 52
Wiesner, M. P., Lin, H., & Soares-Santos, M. 2015, MNRAS, 452, 701
Yang, X., Mo, H. J., van den Bosch, F. C., et al. 2007, ApJ, 671, 153
Yee, H. K. C., & Ellingson, E. 2003, ApJ, 585, 215
Zhang, Y., Jeltema, T., Hollowood, D. L., et al. 2019, MNRAS, 487, 2